

Heat transfer modelling in a rotating cavity using the SST $k-\omega$ turbulence model

W. WRÓBLEWSKI, D. FRĄCZEK

*Institute of Power Engineering and Turbomachinery
Silesian University of Technology
44-100 Gliwice, Poland*

e-mails: wlodzimierz.wroblewski@polsl.pl, daniel.fraczek@polsl.pl

HEAT TRANSFER SIMULATION in a cylindrical cavity rotating around its axis and limited by two metal discs were presented. The object of the calculations was to compare the shear stress transport $k-\omega$ (SST $k-\omega$) turbulence model with the renormalization group $k-\varepsilon$ and $k-\omega$ turbulence models. The calculation results were compared with the results of experiments described in literature. Values of the Nusselt number for the cavity walls were compared depending on three dimensionless numbers used to describe heat transfer in a cavity: the Grashof number Gr and the Reynolds numbers Re_z and Re_ϕ . Flow structures in a rotating cavity were compared for selected thermal and flow conditions. The computations were performed using the ANSYS CFX 14 commercial code.

Key words: rotating cavity, heat transfer, SST, turbulent flow.

Copyright © 2014 by IPPT PAN

Notations

a	inlet opening radius, mm,
b	cavity outer radius, mm,
d	disc thickness, mm,
Bo	natural convection participation $Gr/(Re_z)^2$,
Gr	Grashof number, $\beta_1 \Delta T Re_\phi^2$,
h	specific static enthalpy, J/kg,
\tilde{I}	identity tensor,
Nu	Nusselt number, $qb/\lambda\Delta T$, Nu_{avg} , farthing Nusselt number, $q_{avg}b/\lambda_1(T_1 - T_{s,avg})$,
p	pressure, Pa,
Re_z	axial Reynolds number, $v_a a/\nu$,
Re_ϕ	rotational Reynolds number, $\Omega b^2/\nu$,
s	cavity length, mm,
T	temperature, K,
ΔT	temperature difference $T_1 - T_{sh}$,
t	time, s,
Δt	single-time step, s,
v_r, v_ω, v_a	circumferentially averaged relative velocity: radial, circumferential, axial, m/s,
r	radial coordinate relative to the axis, m,

q	area average heat flux, W/m^2 ,
β	air expansion coefficient, $1/\text{K}$,
Ω	cavity angular velocity, rad/s ,
ρ	density,
λ	thermal conductivity, $\text{W}/\text{m} \cdot \text{K}$,
μ	dynamic viscosity, $\text{Pa} \cdot \text{s}$,
μ_t	turbulent dynamic viscosity, $\text{Pa} \cdot \text{s}$,
ν	kinematic viscosity μ/ρ , m^2/s ,
ν_t	turbulent viscosity μ_t/ρ , m^2/s .

Subscripts

1	parameter at the inlet,
avg	surface radially averaged value,
s	disc body,
sh	parameter at the cavity outer radius (shroud).

1. Introduction

PROVIDING THE AIR FLOW TO DIFFERENT COMPONENTS of the engine through an internal system of passages is an essential problem in the construction of modern turbine engines operating under heavy loads and intended for the aircraft industry. The purpose of the air is to cool components such as discs, blades, bearings or sealing elements. In order to do so, the air is extracted from the compressor. In state-of-the-art structures the cooling air flows to further parts of the engine through the passage in the high-pressure compressor rotor drum. This is shown on the diagram in Fig. 1. The drum is a disc structure and the discs have a central opening through which the cooling air flows. There are cavities between the discs. Because the mass flow of the cooling air usually constitutes several percent of the main mass flow, it has an essential impact on the efficiency of the entire turbine. Therefore the minimization of the inside air mass flow and

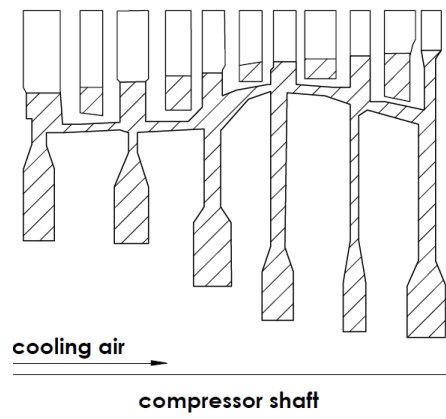


FIG. 1. Simplified longitudinal section of a high-pressure axial compressor.

proper streamlining of its spread are important and must be based on detailed knowledge of heat transfer conditions and of the flow field.

The air flowing through the middle passage in the compressor drum penetrates the cavities located between the discs. The inertial forces affecting the gas, which result from the rotational motion and the convective heat flow, create flow structures inside the cavities. Depending on conditions, these may feature varied eddy structures composed of pairs of concurrent and countercurrent vortices. The air flow and the heat transfer processes are unsteady and relatively complex. Due to the nature of the heat transfer, the flow field may be divided into free, intermediate and forced convection areas.

The phenomena that occur in rotating cavities are identified both experimentally and numerically [1–5]. Due to the non-stationary nature of these phenomena and because of the complexity of flow structures, it is difficult to carry out experimental testing. The measurement of necessary parameters is complicated and sometimes impossible to be carried out directly. Numerical computations are important supplement to experimental testing. It is essential here that the employed numerical model should allow possibly close simulations of the real thermal and flow processes that occur in the rotating cavity. Statistical turbulence models are used in many analyses of such phenomena. Typically, it is the $k-\varepsilon$ turbulence model that is applied [1–3, 6, 7]. In present technical applications one of the most popular models used to simulate the complex flow phenomena is the shear stress transport $k-\omega$ (SST $k-\omega$) turbulence model [8–11]. So far, however, this model has been used to solve problems related to rotating cavities in a limited manner. One of the few examples where it was employed is presented in [12]. The SST $k-\omega$ and the $k-\varepsilon$ models were compared In this work with the Reynolds stress model (RSM). The rotor-stator configuration of the cavity of the SST $k-\omega$ model featured the best ratio of accuracy to the required computing power.

Attempts are made to solve the phenomena occurring in rotating cavities by using both stationary and non-stationary models. It is stated in [13] that main flow instabilities take place in areas with large angular velocity gradients. OWEN [14] tried to define the laws that have a decisive impact on the exchange of mass and energy inside a cavity. According to him, the state prevailing in this system is one of non-equilibrium and the system tends to maximize the flow of entropy and matter, which allows it to maintain stability. Based on the analysis of previous works [15], he states that a system may have several temporary solutions and a single global solution. What was to decide about the nature of the flow was the number of pairs of vortices arising in the cavity and referred to as the Bénard cells. This number was a function of the gas rotational and axial velocity and the wall temperature distribution. Due to the regularity of the solutions that arose, Owen stated that it could be appropriate for the analysis to use a set of stationary equations instead of non-stationary ones.

Because the flow area of the model cavity has a relatively simple shape, there are attempts to model flow phenomena in a rotating cavity by means of the direct numerical simulation (DNS) method and variants of the large eddy simulation (LES) method [16–18]. Due to computing time, the use of the DNS model makes sense only for relatively low Reynolds numbers and it is especially useful for testing the stability of flow structures arising in the vicinity of a rotating disc. The LES method is less time-consuming and more often used to simulate phenomena in a rotating cavity. In [1] the results obtained using the $k-\omega$ turbulence model were compared with the ones produced by the LES method. The LES method had better correlation with experimental results. In spite of this, modelling by means of the LES method is not used in engineering practice at present, especially for purposes related to diagnostics or adjustment, due to the amount of time which is required. These cases require a much faster solution to a given flow problem.

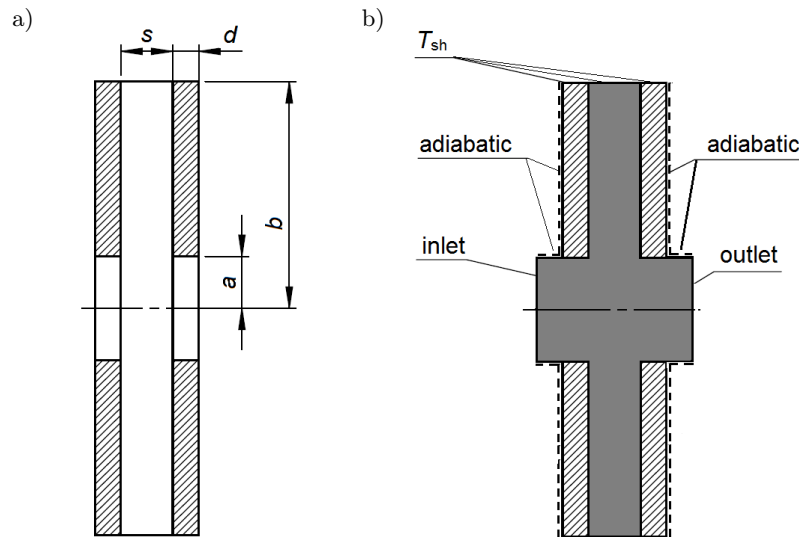


FIG. 2. Geometrical model of the cavity (a) and computational areas (b).

Experimental testing makes use of the relationships between boundary conditions and the flow structure. They are expressed by the following dimensionless numbers: the rotational and axial Reynolds numbers (Re_ϕ , Re_z) and the Grashof number (Gr). The results of a series of experiments concerning heat transfer in a rotating cavity were presented by FARTHING *et al.* in [5]. The measurements were made in the range of Reynolds numbers of $2.0 \cdot 10^5 \leq Re_\phi \leq 5.0 \cdot 10^6$; $2.0 \cdot 10^4 \leq Re_z \leq 1.6 \cdot 10^5$ and the Grashof numbers of $1.0 \cdot 10^{10} \leq Gr \leq 7.5 \cdot 10^{12}$. The results predicted that for a symmetrical heating of discs, the range of varia-

tion in the Nusselt number on the walls of both discs was similar. The values of the Nusselt number grow as the values of Re_ϕ and Re_z got higher, reaching the maximum of approximately $Nu = 200$. If one of the discs was not heated, the differences between the heat flux values on the walls would rise, but the distribution of the Nusselt number on the heated disc would remain similar to the one obtained if the cavity was heated symmetrically. In their work Farthing *et al.* indicated that the radial heat flow was almost none when the cavity was heated symmetrically, whereas this flow was significant in non-symmetrical cases. Two models were analyzed: with the ratio of dimensions $s/b = 0.138$ with no shaft and $s/b = 0.267$ with a central shaft (cf. Fig. 2). They showed that neither additional presence of the shaft in the rotor axis nor the proportion of the inlet gap to the cavity height had an impact on the value of the Nusselt number.

For the purposes of numerical analyses presented in literature, the rotating cavity is often defined in a simplified manner. A single cavity is separated from the compressor rotor drum and it is assumed that the limiting walls are flat. This allows an easier discretization of the computational domain, an acceleration in the time needed for computations and a construction of experimental models at lower costs. In [4] numerical studies were conducted on the impact of geometry on the heat flow and on the flow structures arising in the cavity. The obtained results showed that the heat fluxes from the cavity walls depended predominantly on the amount of the fluid separated from the main axial flow and moving into the cavity. The narrowing of the passage resulting from the presence of the machine shaft changed the heat flux by about 14%, which was not confirmed by the experiments described in [5]. In some cases ($s/b = 0.36$) symmetry in convective flows inside the cavity was found.

TIAN *et al.* [3] analyzed the numerical model of the flow of mass and energy in a rotating cavity using geometrical data from the experiment described by FARTHING *et al.* in [5]. In their calculations they adopted the stationary flow model and employed the $k-\varepsilon$ turbulence model. The computations were performed for the following ranges: $2.81 \cdot 10^7 \leq Gr \leq 6.89 \cdot 10^9$; $1.34 \cdot 10^4 \leq Re_z \leq 1.14 \cdot 10^5$; $1.29 \cdot 10^4 \leq Re_\phi \leq 5.00 \cdot 10^6$, for which a change in the heat transfer conditions from free convection to forced convection occurs. The presented results indicated that in areas distant from the flow axis the heat transfer was dominated by free convection but in areas close to the axis – forced convection prevailed. The factors that determined the intensity of the occurring phenomena were the values of individual Re and Gr numbers. It was found that for $Re_z = 1.34 \cdot 10^4$ free convection played a decisive role in the heat transfer. As the value of Re_z rises, with unchanged values of the remaining numbers, the role of forced convection in the heat transfer becomes more important. Similar results were obtained for a rotating cavity by OWEN *et al.* [6], who used the RNG $k-\varepsilon$ turbulence model in their calculations.

In this paper, the flow through a rotating cavity was modelled by means of the non-stationary flow model and the SST $k-\omega$ model was used as the main model of turbulence. The ANSYS CFX 14 commercial software package was used for the analyses. The heat transfer conditions were assessed in a relatively wide range of dimensionless numbers. The values of the Grashof number were assumed in the range of $1.01 \cdot 10^9 \leq Gr \leq 3.37 \cdot 10^{11}$ and of the Reynolds numbers – in the ranges of $2.69 \cdot 10^4 \leq Re_z \leq 4.02 \cdot 10^5$ and $7.73 \cdot 10^4 \leq Re_\phi \leq 1.41 \cdot 10^6$. The results of the computations were compared with experimental data and calculation results described in literature to determine the suitability of the SST $k-\omega$ turbulence model for the identification of thermal and flow phenomena in rotating cavities.

2. Model description

2.1. Mathematical model

The computational area in the problem under consideration is composed of the fluid domain and the solid domain. In the fluid domain area the mass, momentum and energy conservation equations are solved in the form of unsteady Reynolds-averaged Navier–Stokes (URANS) equations. The high-order advection scheme and the second order backward Euler transient scheme were used.

For the conjugate heat transfer (CHT) analysis, the energy equations for the fluid and solid are solved simultaneously using the same numerical algorithm. The total energy equation with the viscous work term was used [19]:

$$(2.1) \quad \frac{\partial(\rho I)}{\partial t} - \frac{\partial p}{\partial t} + \frac{\partial}{\partial x_j}(\rho U_j I) \\ = \frac{\partial}{\partial x_j} \left(\lambda \frac{\partial T}{\partial x_j} + \frac{\mu_t}{Pr_t} \frac{\partial h}{\partial x_j} \right) + \frac{\partial}{\partial x_j} \left[U_j \cdot (\mu + \mu_t) \left(\frac{\partial U_j}{\partial x_i} + \frac{\partial U_i}{\partial x_j} - \frac{2}{3} \frac{\partial U_k}{\partial x_k} \tilde{I} \right) \right],$$

$$(2.2) \quad I = h + \frac{1}{2} U_i U_j - \frac{1}{2} \omega^2 R^2 + k,$$

where the turbulent Prandtl number $Pr_t = 0.9$. This equation is similar for all two-equation turbulence models.

The values of the Reynolds stress in the URANS equations are computed by the SST $k-\omega$ turbulence model. The model is popular in research on flow structures in turbomachines, including those where the heat transfer process is essential [9, 20–23]. The SST $k-\omega$ model is a two-equation model which, in order to determine eddy viscosity, requires solving two additional transport equations: for the turbulence kinetic energy and for the value defining its dissipation. The

model combines the advantages of the k- ε and k- ω model [24]. Turbulence kinematic viscosity is defined as:

$$(2.3) \quad \nu_t = \frac{a_1 k}{\max(a_1 \omega, S F_2)},$$

turbulence kinetic energy:

$$(2.4) \quad \frac{\partial k}{\partial t} + U_j \frac{\partial k}{\partial x_j} = P_k - \beta^* k \omega + \frac{\partial}{\partial x_j} \left[(\nu + \sigma_k \nu_t) \frac{\partial k}{\partial x_j} \right],$$

specific dissipation rate:

$$(2.5) \quad \frac{\partial \omega}{\partial t} + U_j \frac{\partial \omega}{\partial x_j} = \alpha S^2 - \beta' \omega^2 + \frac{\partial}{\partial x_j} \left[(\nu + \sigma_\omega \nu_t) \frac{\partial \omega}{\partial x_j} \right] + 2(1 - F_1) \sigma_\omega \frac{1}{\omega} \frac{\partial k}{\partial x_j} \frac{\partial \omega}{\partial x_j}.$$

Variable k determines the turbulence energy and ω , also known as the turbulence frequency, determines the turbulence scale. P_k is the product of k and S is the magnitude of the strain rate. Blending functions F_1 and F_2 are used in the SST k- ω model. The functions activate the k- ω model in the vicinity of the wall and the k- ε model – in the remaining part of the flow. A detailed description of this turbulence model can be found in [19] and [25].

As it was shown [16], the value of the turbulence kinetic energy has an impact on the obtained values of the heat flux from the wall to the fluid. KATO and LAUNDER [26] noticed that the very high levels of the shear strain rate in stagnation regions were responsible for the excessive levels of the turbulence kinetic energy. Turbulence production P_k can be expressed as follows [25]:

$$(2.6) \quad P_k = \mu_t \left(\frac{\partial U_i}{\partial x_j} + \frac{\partial U_j}{\partial x_i} \right) \frac{\partial U_i}{\partial x_j} - \frac{2}{3} \frac{\partial U_k}{\partial x_k} \left(3\mu_t \frac{\partial U_k}{\partial x_k} + \rho k \right).$$

Kato and Launder proposed a modified value of the turbulence production limiter, which they linked to the vorticity rate:

$$(2.7) \quad P_k = \mu_t S \Omega - \frac{2}{3} \frac{\partial U_k}{\partial x_k} \left(3\mu_t \frac{\partial U_k}{\partial x_k} + \rho k \right),$$

$$(2.8) \quad S = \sqrt{2 S_{ij} S_{ij}},$$

$$(2.9) \quad S_{ij} = \frac{1}{2} \left(\frac{\partial U_i}{\partial x_j} + \frac{\partial U_j}{\partial x_i} \right),$$

$$(2.10) \quad \Omega = \sqrt{2 \Omega_{ij} \Omega_{ij}},$$

$$(2.11) \quad \Omega_{ij} = \frac{1}{2} \left(\frac{\partial U_i}{\partial x_j} - \frac{\partial U_j}{\partial x_i} \right),$$

where S_{ij} defines the strain rate tensor and Ω_{ij} defines the vorticity tensor.

2.2. Geometrical model and boundary conditions

The volume inside the compressor rotor is usually simplified for the purposes of computational analyses. In the drum there are a number of cavities separated from each other by discs and it may be assumed for the calculations that the phenomena taking place in them occur independently. In order to obtain a geometrical model, a single cavity is separated together with discs limiting it (Fig. 2a). In order to make comparisons, the cavity geometrical data were assumed based on [3]. The cavity dimensions are as follows: inlet $a = 40$ mm, outer radius $b = 175$ mm and cavity length $s = 40$ mm. The cavity length-to-height ratio is $s/b = 0.229$. For simplicity, the discs are in the form of simple rings with thickness $d = 20$ mm with a central hole (Fig. 2). The discs are connected to each other but the connection area is not taken into consideration explicitly in the geometrical model, but only through setting a boundary condition on the outer radius. For such a geometrical model computational areas were defined.

It is assumed in the computational model that the cavity discs are made of metal with a density of 7854 kg/m^3 , a heat conductivity coefficient of $60.5 \text{ W/m} \cdot \text{K}$ and a specific heat capacity of $434 \text{ J/kg} \cdot \text{K}$. The air which flows axially through the central holes is treated as compressible perfect gas. The impact of the gravity force on the phenomena that occur is ignored because the values of the centrifugal force resulting from the rotational motion of the cavity are by an order of magnitude higher than gravitational acceleration. Similar assumptions were also made in [3]. The kinematic viscosity coefficients and the heat conductivity coefficient of air were assumed according to Sutherland's formulae:

$$(2.12) \quad \mu = \mu_0 \left(\frac{T}{T_0} \right)^{3/2} \frac{T_0 + S}{T + S},$$

$$(2.13) \quad \lambda = \lambda_0 \left(\frac{T}{T_0} \right)^{3/2} \frac{T_0 + S}{T + S},$$

where: $\mu_0 = 1.72 \cdot 10^{-5} \text{ Pa} \cdot \text{s}$, $\lambda_0 = 2.36 \cdot 10^{-2} \text{ W} \cdot \text{m}^{-1} \cdot \text{K}^{-1}$, $T_0 = 273 \text{ K}$, $S = 114 \text{ K}$.

It is assumed that the static temperature of air at the inlet is constant and equals $T = 298 \text{ K}$; the value of axial velocity is set depending on the case, according to the assumed dimensionless numbers and using the 1/7 power law inlet velocity profile. The turbulence intensity was $Tu = 5\%$, at $\mu_t/\mu = 10$. The value of the average static pressure at the fluid domain outlet was assumed at $p = 0.1 \text{ MPa}$. The cavity rotational speed was selected for individual cases to ensure a proper value of Reynolds and Grashof numbers. An adiabatic condition was assumed on the outer run-up areas and on the outer surfaces of the disc domains. On the inner walls of the cavity no fluid sliding relative to the walls

was assumed and a convective heat transfer was modelled. The $k-\varepsilon$, $k-\omega$ and SST $k-\omega$ turbulence models were used in the fluid domain. Radiative heat transfer was ignored. On the shroud surface, the wall temperature for the discs and fluid was set at $T_{sh} = 348$ K.

2.3. Computational mesh

The model of the rotating cavity is composed of the fluid domain and two domains of the discs (Fig. 2b). A 3D full 360-degree axisymmetric model was computed. The area of both discs was discretized by means of a structural mesh with uniform resolution. This is sufficient to carry out simulations of the heat transfer in metal. Each area of the discs has 15 120 nodes. The fluid domain is located between the discs and in the central area of the rotor. Mesh domains are shown in Fig. 3.

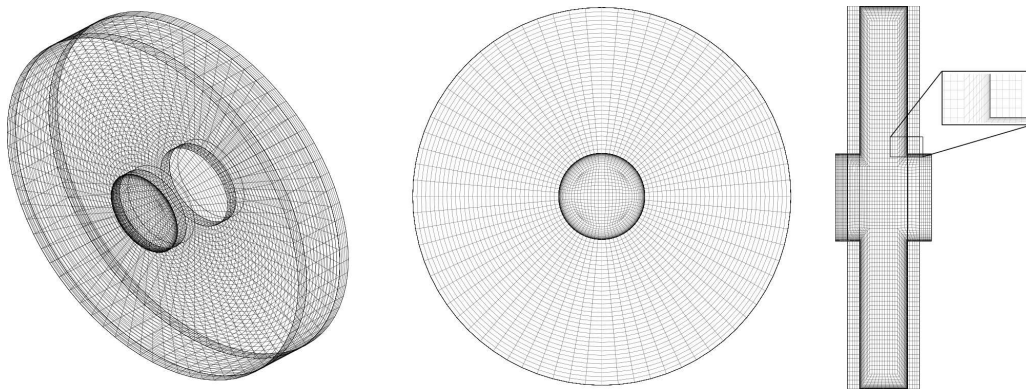


FIG. 3. Computational mesh.

A structural mesh with a concentration of lines in the wall area was used for the calculations in the fluid domain. Fourteen lines were used in the boundary layer near the walls and the maximum value of y^+ – the parameter based on the distance from the wall to the first node and on the wall shear stress parameter values – was smaller than 1.

In order to check whether the solution was independent of the mesh, test calculations were made of the fluid for meshes with a different grid resolution. The grid resolution of the basic mesh with 108 626 nodes for the fluid and the total number of nodes of 138 866 was achieved by increasing the number of nodes in the radial direction, thus obtaining 276 818 and 307 058 nodes, respectively. In the second variant, a fourfold concentration of the mesh was achieved along the cavity perimeter with 666 200 and 670 904 nodes, respectively. Figure 4 presents the results of comparisons of the distribution of the circumferentially averaged

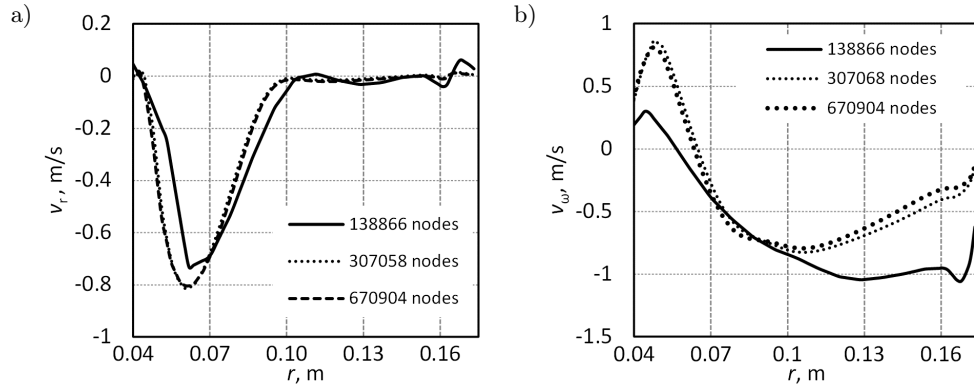


FIG. 4. Comparison of a) v_r and b) v_ω velocity; $Re_z = 4.02 \cdot 10^4$; $Re_\phi = 1.03 \cdot 10^5$, $Gr = 1.82 \cdot 10^9$.

radial and circumferential velocity profiles (taken at the symmetry plane of the cavity) which indicate that the velocity distributions obtained with the mesh with a fourfold concentration are only slightly different compared to those obtained with the mesh with a twofold concentration. The results obtained for the mesh with the smallest number of nodes differed substantially. Considering this, a mesh with 307 058 nodes was adopted for further computations. The time-step level was based on the advection scale ($\Delta t = 0.1/\Omega$). The turbulent spectrum was not included to set the time step. Three time steps: $0.25\Delta t$, $0.5\Delta t$ and Δt were compared but no significant differences in the velocity distribution were observed.

3. Calculation results

At first, a series of test calculations was performed for the so-defined model to determine the differences in the solutions obtained for the selected two-equation models: RNG $k-\varepsilon$, $k-\omega$ and SST $k-\omega$. Because stagnation areas may appear in the rotating cavity, the impact of the Kato–Launder formula in the turbulence model was also checked. The following values of the dimensionless numbers were assumed for the calculations: $Re_z = 2.69 \cdot 10^4$; $Re_\phi = 9.41 \cdot 10^5$ and $Gr = 1.49 \cdot 10^{11}$.

In each case, stationary calculations were made first. They were used as the input conditions for non-stationary analyses. All simulations were carried out for the non-stationary flow model. The time step was selected at the level of up to $2 \cdot 10^{-4}$ s.

The performed non-stationary calculations resulted in a periodical variability of parameters in time. The curves illustrating changes in Nu depending on time

for a selected time range are presented in Fig. 5. Oscillations in the heat flux occur for all models but the frequencies, amplitudes and average values of these changes vary depending on the turbulence model. FFT analysis (for $0.5\text{ s} < t$) shows that three main components of Nu oscillation are below 20 Hz for all models. The maximum average values occur for the RNG $k-\varepsilon$ model with the Kato–Launder correction active; they keep Nusselt number value around 145. The minimum average values at the level of $Nu = 101$ occur for the $k-\varepsilon$ model. The highest amplitude is observed for the RNG $k-\varepsilon$ model and the lowest – for the SST $k-\omega$ model. The application of the Kato–Launder correction stabilizes the heat flux and the frequency of its changes for all turbulence models. The Kato–Launder correction increases the average value of the Nusselt number. For all turbulence models, the average Nusselt number values rise by approximately 40% if the Kato–Launder function is added.

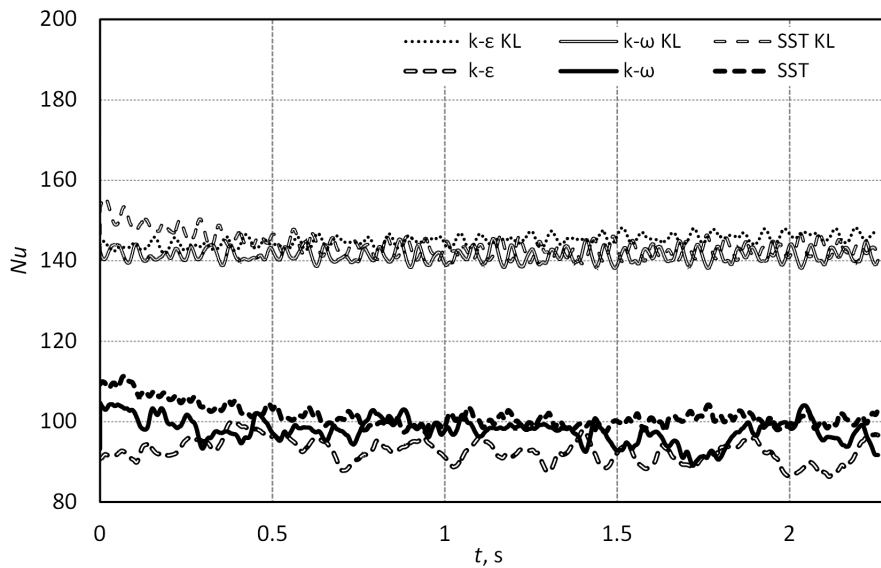


FIG. 5. Nusselt number depending on time for $Re_z = 2.69 \cdot 10^4$, $Re_\phi = 9.41 \cdot 10^5$, $Gr = 1.49 \cdot 10^{11}$.

The differences in the average values of the Nusselt number between individual models are significant and reach as much as 40%. No change was found in time in the number of vortices, whereas such an evolution of structures was suggested in [14] and observed in [27]. Vortex structures were only slipped relative to the cavity walls.

Essential differences can be noticed in the distributions of streamlines of the instantaneous flow field (taken at the symmetry plane of the cavity) presented

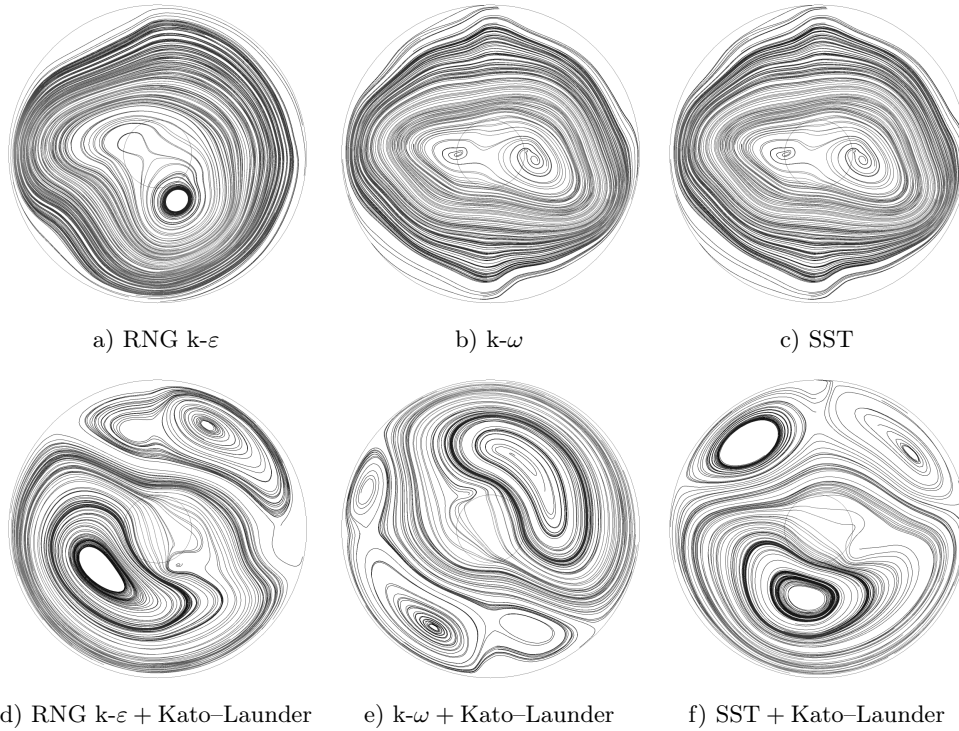


FIG. 6. Comparison of streamlines of instantaneous flow field for different turbulence models; $Re_z = 2.69 \cdot 10^4$, $Re_\phi = 9.41 \cdot 10^5$ and $Gr = 1.49 \cdot 10^{11}$.

in Fig. 6. Depending on the applied turbulence model, the proportions of the concurrent vortices to the countercurrent ones change. Only one vortex is clearly visible for the RNG $k-\varepsilon$ turbulence model. The SST $k-\omega$ model, which is a combination of models $k-\varepsilon$ and $k-\omega$, presents a streamline distribution similar to the $k-\omega$ model. The application of the Kato-Launders correction results in a clearer structure of the countercurrent vortices in all three models.

Higher order statistics were used to analyze the heat flux distribution on the disc and the distributions of averaged velocity components in the symmetry plane. Profiles of the upstream disc circumferentially averaged heat skewness G_1 and kurtosis G_2 were calculated for 2500 iterations and the results are presented in Fig. 7:

$$(3.1) \quad G_1(x) = \frac{n}{(n-1)(n-2)} \sum \left(\frac{x_i - \bar{x}}{s} \right)^3,$$

$$(3.2) \quad G_2(x) = \left\{ \frac{n(n+1)}{(n-1)(n-2)(n-3)} \sum \left(\frac{x_i - \bar{x}}{s} \right)^4 \right\} - \frac{3(n-1)^2}{(n-2)(n-3)},$$

where n is the sample size and s is the sample standard deviation.

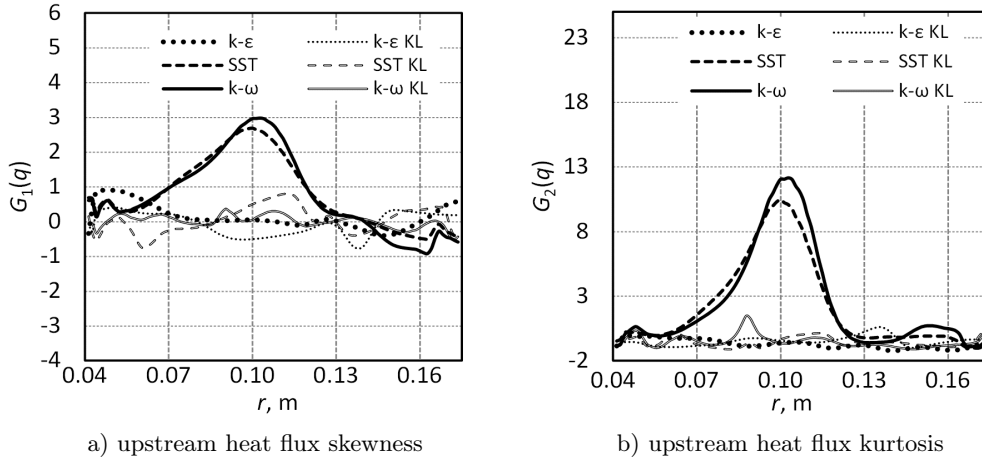


FIG. 7. Disc heat flux skewness and kurtosis for $Re_z = 2.69 \cdot 10^4$, $Re_\phi = 9.41 \cdot 10^5$, $Gr = 1.49 \cdot 10^{11}$.

The skewness and kurtosis for the circumferentially averaged velocity are presented in Fig. 8. The skewness and flatness calculated for the heat flux were similar for both discs. Therefore, only the distributions from the upstream disc are presented. The skewness and the kurtosis distribution for the SST and $k-\omega$ turbulence models are closer than for the other models. Clear maximum values of skewness and kurtosis occur on the radius of 0.1 m for the SST and $k-\omega$ models. The skewness values suggest that heat fluxes for the SST and $k-\omega$ turbulence models had an asymmetrical distribution and were dominated by heat fluxes lower than mean values. The kurtosis of the heat flux shows that fluctuations occurred mostly for the $k-\varepsilon$ turbulence model and for models with the production limiter. The production limiter reduces values of skewness, which suggests that the heat flux distribution is more symmetrical. Comparisons of the radial and axial velocity kurtosis indicate that the production limiter is responsible for flattening velocity fluctuations.

Considering that the phenomena in the cavity are substantially affected by the flow inner structures, and it is the $k-\omega$ model that dominates in these areas, and due to the very small values of velocity in the cavity (low velocity gradients), a decision was made not to use the Kato–Launder correction in further analyses.

In the next stage, a computational analysis was conducted to compare variations in the values of heat fluxes obtained for the SST $k-\omega$ turbulence model as a result of a change in the rotational speed of the cavity and in the flow rate of the air flowing through it. The obtained results are compared with the results of experimental testing [5] and those presented in [3]. The varying operating conditions are defined by means of dimensionless numbers. The computations were

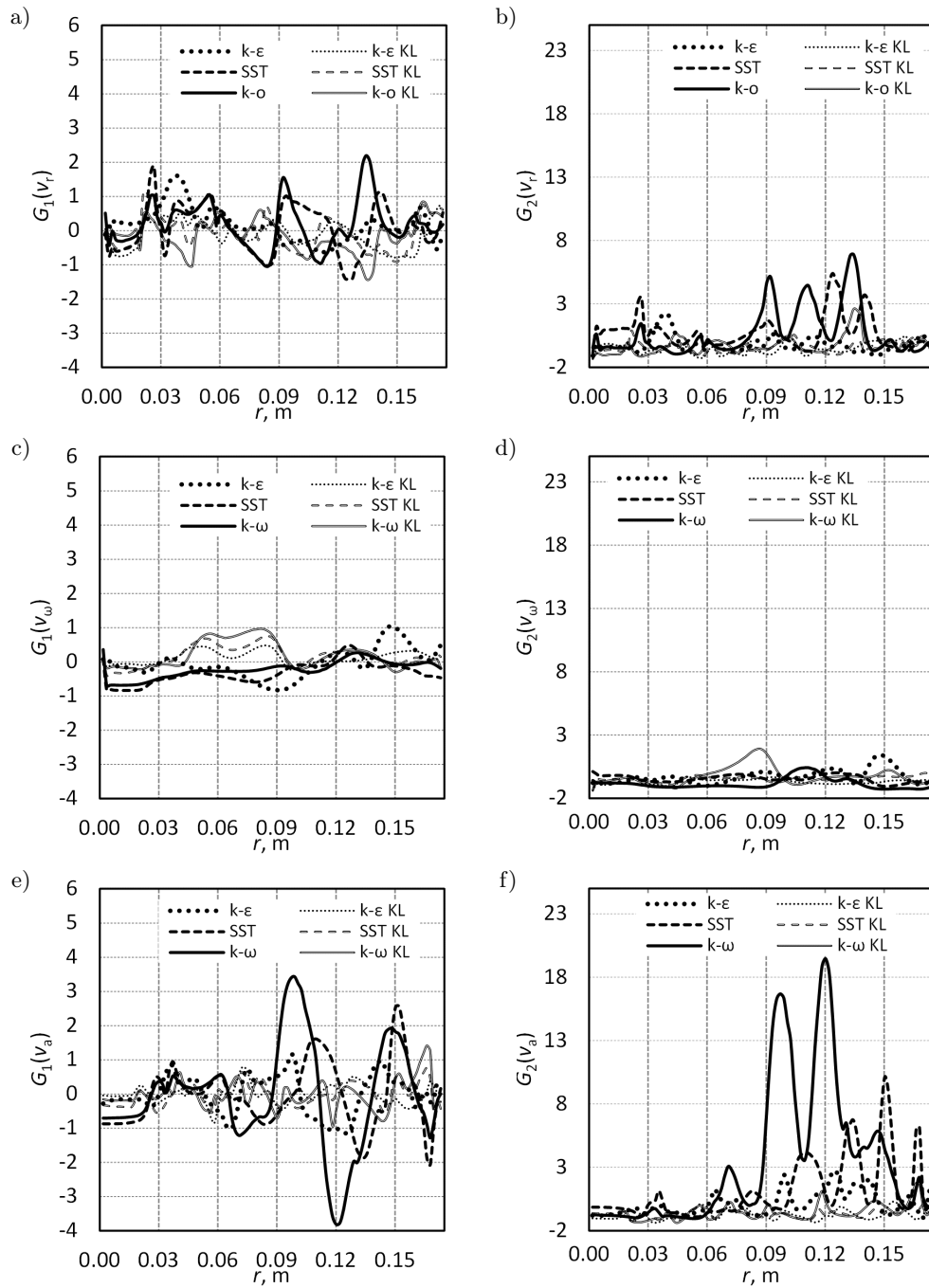


FIG. 8. Skewness and kurtosis for v_r , v_ω , v_a , $Re_z = 2.69 \cdot 10^4$, $Re_\phi = 9.41 \cdot 10^5$, $Gr = 1.49 \cdot 10^{11}$.

performed for the Reynolds number range of $2.69 \cdot 10^4 < Re_z < 4.02 \cdot 10^4$ and that of the Grashof number of $1.0 \cdot 10^9 < Gr < 3.37 \cdot 10^{11}$.

The average value from last several periods of changes was used to compare the values of the Nusselt number. The entire physical time of the simulation takes a few seconds.

TIAN *et al.* [3] suggested that for certain values of Re_z and product $\beta \cdot \Delta T$ the Nusselt number should be made dependent on the Grashof number only. Under these assumptions, the situation comes down to linking Nu to Re_ϕ only (by definition $Gr = \beta \Delta T (Re_\phi)^2$). For the assumed values of $Re_z = 2.69 \cdot 10^4$, $\beta \Delta T = 0.169$, $1.12 \cdot 10^5 < Re_\phi < 2.02 \cdot 10^5$ they proposed the following equation for the Nusselt number:

$$(3.3) \quad Nu = 36.424 \cdot \left(\frac{Gr}{10^9} \right)^{0.296}.$$

The range of $1.12 \cdot 10^5 < Re_\phi < 2.02 \cdot 10^5$ in Eq. (3.3) corresponds to the change in the Grashof number in the range of $2.13 \cdot 10^9 < Gr < 6.89 \cdot 10^9$. The slight impact of Re_z on the heat flux in the range of $Re_z < 4 \cdot 10^5$ was confirmed by the results of experimental testing in [5]. For this sort of range of dimensionless Gr and Re_z , the value of the Nusselt number depends mainly on the cavity rotational speed represented by Re_ϕ . Similar conclusions were also formulated in [28].

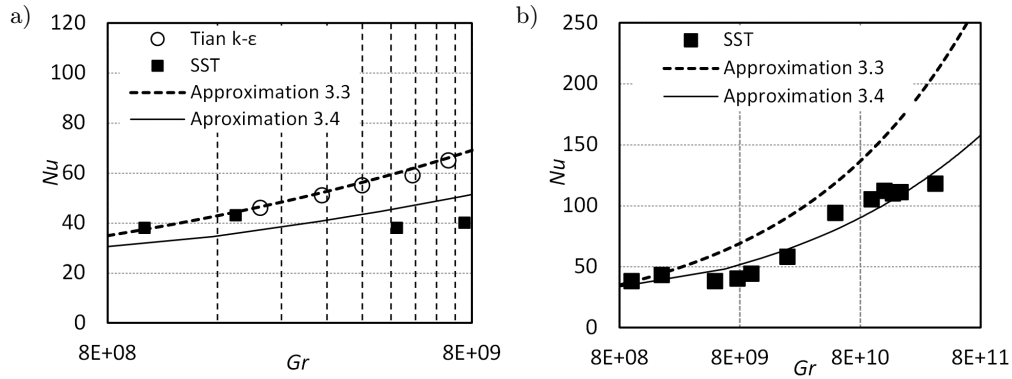


FIG. 9. Comparison of calculation results for the SST $k-\omega$ turbulence model with those in [3] for the range of the Grashof number of a) $1 \cdot 10^9 < Gr < 9 \cdot 10^9$, b) $1 \cdot 10^7 < Gr < 3.37 \cdot 10^{11}$.

Figure 9 presents a comparison of the average value of the Nusselt number with calculation results obtained in [3], based on Eq. (3.3). Figure 9a presents a comparison for smaller values of the Grashof number included in the range of $1 \cdot 10^9 < Gr < 8 \cdot 10^{10}$, for which Tian made the calculations (using the $k-\epsilon$

turbulence model). For values up to $Gr = 5 \cdot 10^5$, a good compliance is observed between the results obtained from calculations using the SST $k-\omega$ model and those produced using the $k-\varepsilon$ turbulence model. In the area for $Gr > 5 \cdot 10^9$, the calculated values begin to differ from obtained in [3] results and, consequently, from what is presented in the graph of Eq. (3.3).

Based on the conducted numerical analyses, an approximation equation was put forward:

$$(3.4) \quad Nu = 30.99 \cdot \left(\frac{Gr}{10^9} \right)^{0.243}.$$

It should be remembered that Eq. (3.3) was selected for the range of $Gr < 6.89 \cdot 10^9$. The calculations made for this range predicted the values obtained by means of the SST model diverged only slightly from the results given in [3]. In an extended range of changes in the Grashof number, which was not analyzed in [3], the approximation equation gives values by about 30–40% higher than the calculated ones.

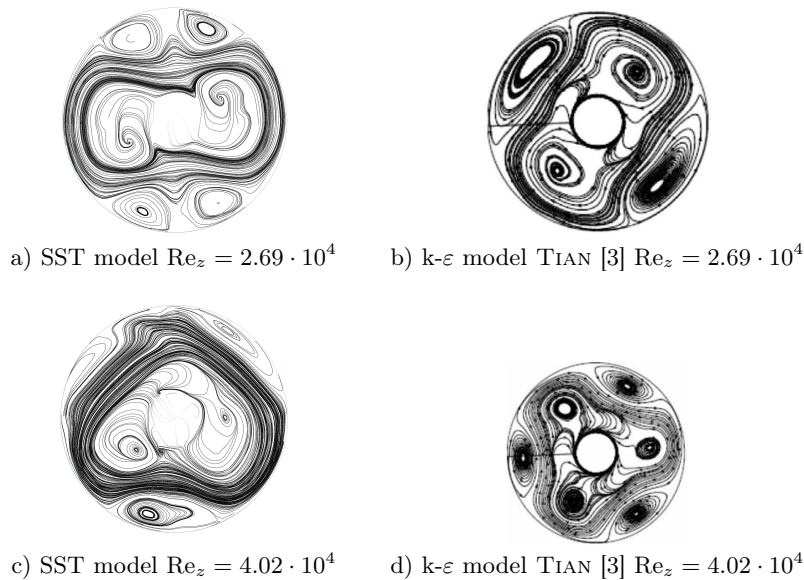


FIG. 10. Comparison of streamlines of instantaneous flow field in the cavity section for SST $k-\omega$ and $k-\varepsilon$ models [3] for different values of Re_z , $Re_\phi = 1.03 \cdot 10^5$.

The flow structures arising in the cavity have an essential impact on the heat transfer conditions. Mapping them as accurately as possible by means of computational models is crucial for a correct quantitative assessment of the conditions prevailing in the rotor drum. Figure 10 presents a comparison of the

structures of the vortices arising in the cavity. The vortex structures are shown in cross-section halfway along the cavity length for two characteristic cases and compared with the structures obtained in [3]. Figures 10a and 10b compare the structures obtained for $Re_z = 2.69 \cdot 10^4$. Two pairs of vortices can be observed in this case. The image of these vortices obtained from calculations using the SST $k-\omega$ model is very similar to the result produced in [3] by means of the $k-\varepsilon$ model. The flow is dominated by forced convection in the vicinity of the cavity axis. Free convection, which can be identified by the formation of pairs of vortices, occurs in the area close to the shroud. The results obtained for both models – the SST $k-\omega$ and the $k-\varepsilon$ – indicate that vortices cover the entire height of the cavity and cause a heat transfer from the shroud area towards the axis.

Figures 10c and 10d present the structures obtained for $Re_z = 4.02 \cdot 10^4$. There are three pairs of vortices in this case and the impact of forced convection on heat exchange becomes higher. The heat transfer resulting from free convection and mixing of the fluid flowing in the axis area with the fluid inside the cavity becomes more difficult. The second case indicates that if both forced and free convection are mapped, the SST $k-\omega$ model smooths over the border between these areas and changes the proportions of the size of the pairs of vortices to each other. The radial arm convection structures which are obtained by means of the $k-\varepsilon$ model intensify flows in the cavity and consequently improve heat transfer conditions compared to the SST $k-\omega$ model. In the case of the SST turbulence model, the structure is dominated by vortices located closer to the cavity axis and rotating in same direction as the cavity, which may justify the differences between the values of Nu (Fig. 9) for higher values of Gr.

Figure 11 presents a comparison of the distributions of circumferentially averaged radial velocity v_r and circumferential velocity v_θ obtained for the SST $k-\omega$ turbulence model with the results obtained by the $k-\varepsilon$ turbulence model. In this case, the maximum differences between the values of the relative velocity components obtained for different turbulence models amount to 35% for the radial and 80% for the circumferential component. The maximum of the radial component for the SST $k-\omega$ model is shifted towards bigger radii. For the circumferential component this shift is slight. For a higher value of $Re_z = 4.02 \cdot 10^4$, the differences between the values of the velocity radial components fade away, whereas the differences in circumferential components reach 40% (Fig. 12). Like in the previous case, a shift in the maximum value of velocity was observed for the circumferential component. As Re_z rose, the difference between solutions got smaller.

FARTHING *et al.* [5] conducted experimental testing of heat transfer conditions in a rotating cavity. They presented the distribution of the Nusselt number depending on Re_ϕ in ranges for which free convection played the dominant role in

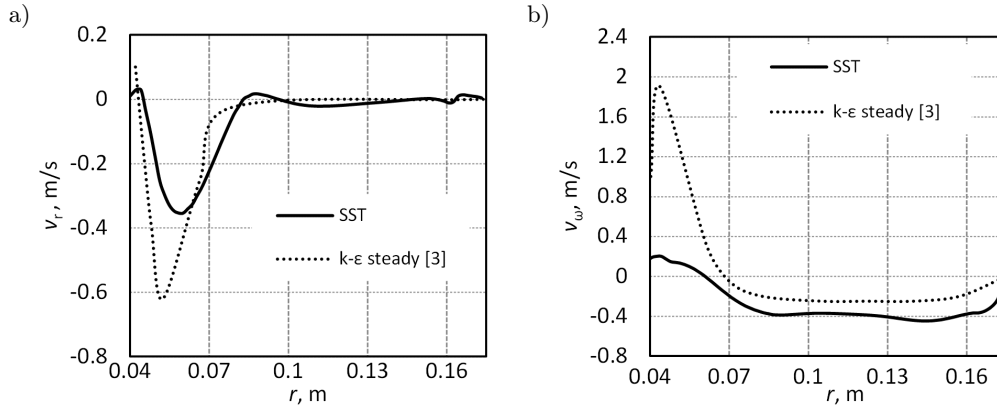


FIG. 11. Comparison of averaged v_r , v_ω velocity distribution; $Re_z = 2.69 \cdot 10^4$, $Re_\phi = 1.03 \cdot 10^5$.

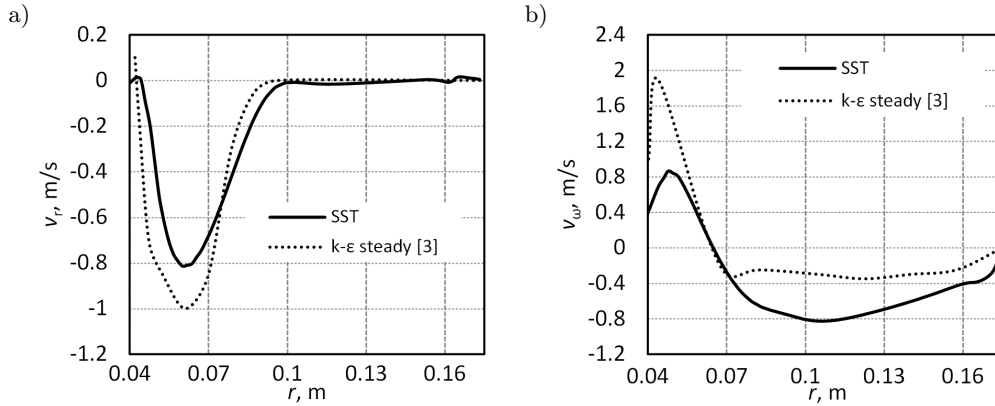


FIG. 12. Comparison of averaged v_r , v_ω velocity distribution; $Re_z = 4.02 \cdot 10^4$, $Re_\phi = 1.03 \cdot 10^5$.

the heat transfer ($Bo > 1$) Buoyancy parameter Bo determines the free-to-forced convection ratio. They found that for $Re_\phi < 5 \cdot 10^5$ the value of Re_z had no effect on the heat flux transferred from the walls to the fluid. Systematic research conducted by FARTHING *et al.* provided reference material for computations by means of the SST $k-\omega$ turbulence model. Figure 13 presents a comparison of the results of the average Nusselt number calculations with experimental results in the range of $2 \cdot 10^5 < Re_\phi < 1.4 \cdot 10^6$. It can be noticed that there is very good agreement between the calculations and the experimental results in the entire range of changes in Re_ϕ under analysis. The heat transfer under the dominance of free convection is mapped correctly.

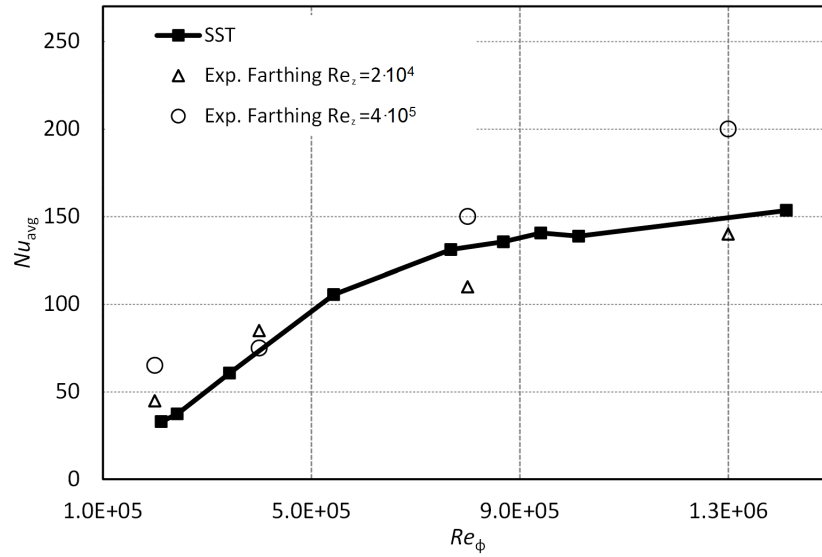


FIG. 13. Comparison of Nu_{avg} with experimental results [5]; $Re_z = 2.69 \cdot 10^4$, $1.0 \cdot 10^9 < Gr < 3.37 \cdot 10^{11}$.

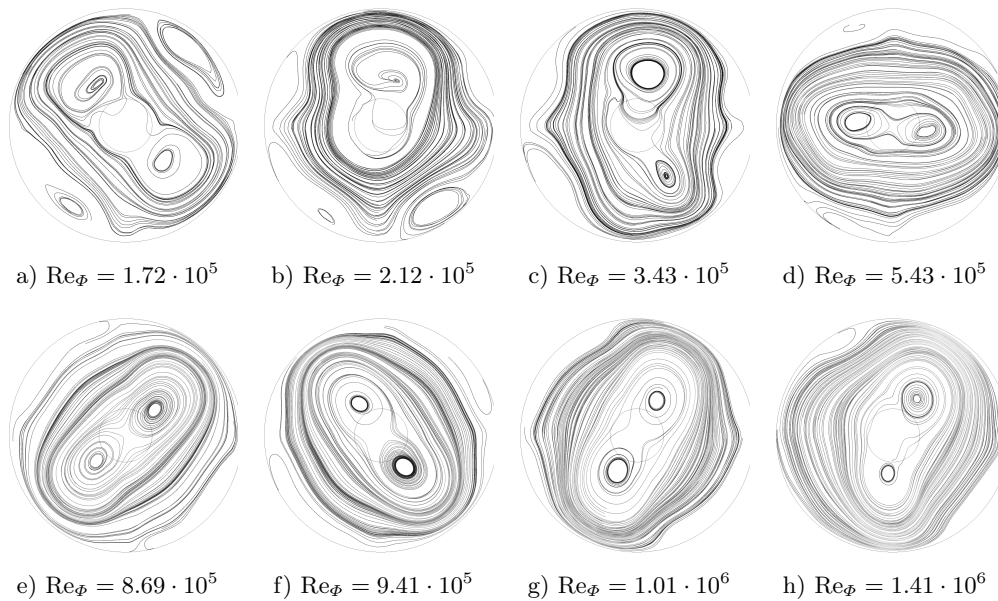


FIG. 14. Change in the vortex structure with a rise in Re_ϕ , $Re_z = 2.69 \cdot 10^4$.

Figure 14 presents distributions of streamlines of instantaneous flow field in the mid-cross section of the cavity obtained from calculations for different values

of Re_ϕ . The other boundary conditions and the turbulence model (SST $k-\omega$) are similar to those presented in Fig. 13. For lower values of Re_ϕ , small vortex structures, which are characteristic of free convection, can be seen near the cavity outer casing. As rotational speed rises, with Re_z maintained, the vortices near the cavity outer casing fade away. The fluid area is dominated by two central vortices. The central vortices are related to forced convection. They transport air from the outer surface region towards the rotation axis.

4. Conclusions

An analysis of the results of numerical calculations of a non-stationary spatial flow field in a rotating cavity was presented. The model takes into account the conjugation of the fluid area with the metal area of the discs limiting the cavity. The SST $k-\omega$ and the RNG $k-\varepsilon$ turbulence models were used for the computations. The impact of the Kato–Launder correction in the turbulence model was checked. The calculation results for different dimensionless numbers Re_z , Re_ϕ and Gr were compared with the experimental and numerical computation results presented in literature.

There were quite considerable differences between the average values of the Nusselt number on the disc surface which were obtained from calculations performed using different turbulence models. The maximum differences reached 40%. After the Kato–Launder correction was introduced into the turbulence model, the amplitude of the changes in the Nusselt number was reduced in the $k-\omega$ and the $k-\varepsilon$ turbulence models, the streamline image featured clearly visible pairs of vortices with a similar structure for each of the models. Higher order statistics showed some correlation for the heat flux and velocity distribution over iteration for the SST and the $k-\omega$ turbulence models. After the Kato–Launder production limiter was introduced into solved equations, the differences in the heat and flow distribution and results between the analyzed turbulence models became smaller.

After the Nusselt numbers obtained from the calculations using the SST $k-\omega$ model for different values of Re_ϕ were compared, it turned out that for values of $Gr > 5 \cdot 10^9$ the obtained values were lower compared to those determined by the $k-\omega$ turbulence model approximation equation. This difference gets bigger together with a rise in Gr .

Comparing the streamline distribution it can be noticed that the SST $k-\omega$ model smooths over the border between the areas of free and forced convection by changing the proportions of the size of the pairs of vortices.

A good agreement of vortex structures with those obtained in the calculations presented in [3] was found for lower values of Re_z . The differences between the values of averaged components of velocity decrease as the value of Re_z rises.

The results of the calculations performed using the SST $k-\omega$ turbulence model made it possible to achieve a good agreement with the experimental results for higher values of the Grashof number. An approximation formula for the Nusselt number is given for a wider range of values of the Grashof number. It can be stated that the results are a global solution but no change in vortex pairs (evolving in time) was noticed what was observed in earlier CFD analysis [27].

References

1. Z. SUN, L. KLAS, J.W. CHEW, C. YOUNG, *LES and RANS investigations into buoyancy-affected convection in a rotating cavity with a central axial throughflow*, Journal of Engineering for Gas Turbines and Power, **129**, 318–325, 2007.
2. C. YOUNG, G.D. SNOWSILL, *CFD optimization of cooling air offtake passages within rotor cavities*, Journal of Turbomachinery, **125**, no. 2, 380–386, 2003.
3. S. TIAN, Z. TAO, S. DING, G. XU, *Computation of buoyancy-induced flow in a heated rotating cavity with an axial throughflow of cooling air*, International Journal of Heat and Mass Transfer, **51**, no. 3-4, 960–968, 2008.
4. P.G. TUCKER, C.A. LONG, *Numerical investigation into influence of geometry on flow in a rotating cavity with an axial throughflow*, Int. Comm. Heat Mass Transfer, **23**, no. 3, 335–344, 1996.
5. P.R. FARTHING, C.A. LONG, J.M. OWEN, J.R. PINCOMBE, *Rotating cavity with axial throughflow of cooling air: heat transfer*, Journal of Turbomachinery, **114**, no. 1, 229–236, 1992.
6. J.M. OWEN, H. ABRAHAMSSON, K. LINDBLAD, *Buoyancy-induced flow in open rotating cavities*, Journal of Engineering for Gas Turbines and Power: Transactions Of ASME, **129**, 893–900, 2006.
7. H. IACOVIDES, J.W. CHEW, *The computation of convective heat transfer in rotating cavities*, International Journal of Heat and Fluid Flow, **144**, no. 2, 146–154, 1993.
8. M. MOSHFEGHI, Y.J. SONG, Y.H. XIE, *Effects of near-wall grid spacing on sst- $k-\omega$ model using NREL Phase VI horizontal axis wind turbine*, Journal of Wind Engineering and Industrial Aerodynamics, **107**, 94–105, 2012.
9. W. WRÓBLEWSKI, S. DYKAS, K. BOCHON, S. RULIK, *Optimization of tip seal with honeycomb land in LP counter rotating gas turbine engine*, TASK Quarterly: Scientific Bulletin of Academic Computer Centre in Gdansk, **14**, no. 3, 189–207, 2010.
10. Y.S. TSENG, Y.M. FERNG, C.H. LIN, *Investigating flow and heat transfer characteristics in a fuel bundle with split-vane pair grids by CFD methodology*, Annals of Nuclear Energy, **64**, 93–99, 2014.
11. R. LANZAFAME, S. MAURO, M. MESSINA, *Wind turbine CFD modeling using a correlation-based transitional model*, Renewable Energy, **52**, 31–39, 2013.
12. S. PONCET, R. DA SOGHE, B. FACCHINI, *RANS modeling of flow in rotating cavity system*, Eccomas CFD 2010, Lisbon, 2010.
13. P.G. TUCKER, *Temporal behavior of flow in rotating cavities*, Numerical Heat Transfer, Part A: Applications, International Journal of Computation and Methodology, **66**, no. 12, 611–627, 2002.

14. J.M. OWEN, *Thermodynamic analysis of buoyancy-induced flow in rotating cavities*, Journal of Turbomachinery: Transactions of the ASME, **132**, no. 2, 2010.
15. M.P. KING, M. WILSON, J.M. OWEN, *Rayleigh–Bénard convection in open and closed rotating cavities*, Journal of Engineering for Gas Turbines and Power, **129**, no. 2, 305–311, 2007.
16. E. TULISZKA-SZNITKO, W. MAJCHROWSKI, K. KIELCZEWSKI, *Investigation of transitional and turbulent heat and momentum transport*, International Journal of Heat and Fluid Flow, **35**, 52–60, 2012.
17. A. DRIES, M. OULD-ROUISS, A. MAZOUZ, *Numerical predictions of turbulent heat transfer for air flow in rotating pipe*, International Journal of Heat and Fluid Flow, **31**, no. 4, 507–517, 2010.
18. E. TULISZKA-SZNITKO, K. KIELCZEWSKI, *Numerical study of the flow structure and heat transfer*, Archives of Mechanics, **65**, 527–548, 2013.
19. C. HIRSCH, *Numerical Computation of Internal and External Flows – Fundamentals of Computational, Fluid Dynamics*, (2nd ed.), Elsevier, 2007.
20. P.G. TUCKER, *Trends in turbomachinery turbulence treatments*, Progress in Aerospace Sciences, 1–32, 2013.
21. H.-J. CHOI, M.A. ZULLAH, H.-W. ROH, P.-S. HA, S.-Y. OH, Y.-H. LEE, *CFD validation of performance improvement of a 500 kW Francis turbine*, Renewable Energy, **54**, 111–123, 2013.
22. L. WANG, S. FU, A. CARNARIUS, C. MOCKETT, F. THIELE, *A modular RANS approach for modelling laminar–turbulent transition in turbomachinery flows*, International Journal of Heat and Fluid Flow, **34**, 62–69, 2012.
23. W. ZHANG, Z. ZOU, J. YE, *Leading-edge redesign of a turbomachinery blade and its effect on aerodynamic performance*, Applied Energy, **93**, 655–667, 2012.
24. F.R. MENTER, M. KUNTZ, R. LANGTRY, *Ten years of industrial experience with the SST turbulence model*, Turbulence, Heat and Mass Transfer, **4**, 2003.
25. F.R. MENTER, *Two-equation Eddy-viscosity turbulence models for engineering application*, AIAA Journal, **32**, no. 8, 1598–1605, 1994.
26. M. KATO, B.E. LAUNDER, *The modelling of turbulent flow around stationary and vibrating square cylinders*, Proc. 9th Symposium on Turbulent Shear Flows, Kyoto, August 1993, pp. 10.4.1–10.4.6.
27. P. TUCKER, C. LONG, *CFD prediction of vortex breakdown in a rotating cavity with an axial throughflow of air*, Int. Comm. Heat Mass Transfer, **22**, no. 5, 639–648, 1995.
28. C.A. LONG, P.R.N. CHILDS, *Shroud heat transfer measurements inside a heated multiple rotating cavity with axial throughflow*, International Journal of Heat and Fluid Flow, **28**, no. 6, 1405–1417, 2007.

Received June 21, 2013; revised version April 8, 2014.
